The Astronomical Journal, 163:164 (12pp), 2022 April https://doi.org/10.3847/1538-3881/ac4e92

Simultaneous Detection of Optical Flares of the Magnetically Active M-dwarf Wolf359

Han-Tang Lin[1], Wen-Ping Chen[1,2], Jinzhong Liu[3], Xuan Zhang[3], Yu Zhang[3], Andrew Wang[4], Shiang-Yu Wang[4], Matthew J. Lehner[4,5,6], C. Y. Wen[4], J. K. Guo[1], Y. H. Chang[1], M. H. Chang[1], Anli Tsai[1], Chia-Lung Lin[1], C. Y. Hsu[1], and Wing Ip[1,7]

[1] Graduate Institute of Astronomy, National Central University, 300 Zhongda Road, Zhongli, Taoyuan 32001, Taiwan; wchen@astro.ncu.edu.tw
[2] Department of Physics, National Central University, 300 Zhongda Road, Zhongli, Taoyuan 32001, Taiwan
[3] Xinjiang Astronomical Observatory, Chinese Academy of Sciences, People's Republic of China
[4] Institute of Astronomy and Astrophysics, Academia Sinica, No. 1, Sec. 4, Roosevelt Road, Taipei 10617, Taiwan
[5] Department of Physics and Astronomy, University of Pennsylvania, 209 South 33rd Street, Philadelphia, PA 19125, USA
[6] Center for Astrophysics, Harvard & Smithsonian, 60 Garden Street, Cambridge, MA 02138, USA
[7] Graduate Institute of Space Science, National Central University, 300 Zhongda Road, Zhongli, Taoyuan 32001, Taiwan
Received 2021 August 17; revised 2022 January 13; accepted 2022 January 13; published 2022 March 11

Abstract

We present detections of stellar flares of Wolf 359, an M6.5 dwarf in the solar neighborhood (2.41 pc) known to be prone to flares due to surface magnetic activity. The observations were carried out from 2020 April 23 to 29 with a 1 m and a 0.5 m telescope separated by nearly 300 km in Xinjiang, China. In 27 hr of photometric monitoring, a total of 13 optical flares were detected, each with a total energy of $\gtrsim 5 \times 10^{29}$ erg. The measured event rate of about once every two hours is consistent with those reported previously in radio, X-ray, and optical wavelengths for this star. One such flare, detected by both telescopes on April 26, was an energetic event with a released energy of nearly 10^{33} erg. The two-telescope light curves of this major event sampled at different cadences and exposure timings enabled us to better estimate the intrinsic flare profile, which reached a peak of up to 1.6 times the stellar quiescent brightness, that otherwise would have been underestimated in the observed flare amplitudes of about 0.4 and 0.8, respectively, with single telescopes alone. The compromise between fast sampling so as to resolve a flare profile versus a longer integration time for a higher photometric signal-to-noise ratio provides a useful guidance in the experimental design of future flare observations.

Unified Astronomy Thesaurus concepts: Stellar flares (1603)

Supporting material: animation

1. Introduction

Solar flares are commonly observed surface phenomena, attributable to acceleration of plasma during magnetic reconnection near sunspots and active regions, that lead to sudden brightening observed in radio, optical, and X-ray wavelengths. While the detailed heating mechanism, i.e., how the magnetic energy is converted to gas kinetic energy is still unclear (Benz & Güdel 2010), it is believed that conductive and radiative processes are involved in the cooling phase. The solar flares are classified by the peak flux in soft X-rays, with the most powerful being class X peaking at $>0.1\,\mathrm{erg\,s^{-1}\,cm^{-2}}$. A typical solar flare releases 10^{29}–10^{32} erg. Rare, major flares, which release a total energy more than $\sim 10^{33}$ erg, are linked to coronal mass ejection events which influence space weather and pose potential hazards to terrestrial environments.

Other stars, notably late-type dwarfs, being largely convective are even more predisposed to flare activity and encompass a larger range of energy output, particularly the young ones with fast rotation rates (Feinstein et al. 2020). Based on the K2 light curves of G- to M-type dwarfs, Lin et al. (2019) conclude that later type stars have higher flare occurrence frequencies but generally with less energetic output. M-dwarf flares with much shorter durations have been detected in millimeter wavelengths (MacGregor et al. 2020). Later spectral types (brown dwarfs) have also shown surface activity (e.g., Rutledge et al. 2000).

Our target, Wolf 359 (GJ 406; CN Leo), at a heliocentric distance of 2.41 pc (Gaia Collaboration et al. 2021), is a known eruptive-type red subdwarf (Kesseli et al. 2019). Previously, six flare events were detected during 12.8 hr of monitoring in radio frequencies, equivalent to 47 events per 100 hr (Nelson et al. 1979). Extreme ultraviolet flare events have been reported to occur at least daily (Audard et al. 2000), and major X-ray flares have also been detected in this star (Liefke et al. 2010). Using ground-based and Kepler/K2 observations combining long- and short-cadence light curves of Wolf 359, Lin et al. (2021) derived a flare occurrence rate of once per day for events with a total flare energies $>10^{31}$ erg, and ten times per year for superflares with released energies $>10^{33}$ erg. Such an activity level is considered high even among known flaring M dwarfs.

Magnetic reconnection may not be limited to surface extrusion as in the case of the Sun. The field lines may be linked to some intricate spin–orbit magnetospheric interaction with close-in companion stars, as in RS Canum Venaticorum or BY Draconi type variables. It is known that newly born stars may anchor their magnetic field to circumstellar disks (Feigelson & Montmerle 1999), with which the entwined field lines are susceptible to reconnection and result in outbursts (10^{36} erg) or in extended flaring loops (Hayashi et al. 1996; Shibata & Magara 2011). Superflare events of red dwarfs are suspected to have similar interactions with orbiting giant exoplanets (e.g., Klocová et al. 2017), though there is so far no definite supporting evidence. Wolf 359 is a fast rotator (Guinan

& Engle 2018; 2.72 day) and is known to host at least two exoplanets (Tuomi et al. 2019). One of these, Wolf 359 c (radius 0.1272 $R_{Jupiter}$) is hot and close in (0.018 au, orbital period 2.88 day) suggestive of a possible spin–orbit tidal lock. In the flare star AD Leo, a periodicity of 2.23 day was inferred and attributed to stellar rotation (Hunt-Walker et al. 2012). However, Lin et al. (2021) found no flare timing in synchronization with the planetary orbital phase in Wolf 359.

Here we report on an optical monitoring campaign of Wolf 359. The star was monitored for one week in 2020 April simultaneously with two telescopes. In addition to reaffirmation of the flare rate, with 13 events detected in 27 observing hours, this paper focuses on one major flare observed by both telescopes, affording the possibility to derive the underlined flare profile, whose amplitude would have been underestimated by any single light curve as a result of finite exposure time. While a flare is quantified by the total released energy (essentially scaled with the amplitude multiplied by the duration), usually an event is recognized mainly by a brightness spike. Our study indicates how intrinsically moderate events could escape detection, and provides guidelines for proper sampling specific to certain profiles in the experimental design.

2. Observations and Data Analysis

2.1. CCD Imaging and Light-curve Extraction

The observations reported here were carried out from 2020 April 23 to 29 simultaneously by the Nanshan One-meter Wide-field Telescope (NOWT) in Xinjiang, and one of the TAOS telescopes, except for the night of April 24 for which the TAOS site was weathered out. The TAOS telescopes, each of f/2 50 cm, used to be installed at Lulin Observatory to catch chance stellar occultation events by transneptunian objects (e.g., Alcock et al. 2003; Zhang et al. 2013). Two of the original four TAOS telescopes were relocated in the spring of 2020 to Qitai Station in Xinjiang, some 300 km from Nanshan, also operated by Xinjiang Astronomical Observatory.

The NOWT was equipped with an E2V back-illuminated CCD203-82 camera, with 12 micron pixels, spanning 1.″13/pixel on the sky. For the data reported here, the NOWT observed Wolf 359 in the *R* band for the first five nights, and in the *V* band for the rest two nights. The exposure time was 18 s, with a dead time of approximately 12 s between exposures, amounting to a cadence of ∼30 s.

The TAOS telescope was equipped with a Spectral Instrument 800 camera with 13.5 micron pixels and a plate scale of 2.″78/pixel. A custom-made filter was used which has a flat-response in 500–700 nm approximately comparable to an SDSS r' filter. For the observing campaign of Wolf 359, the exposure time was 45 s, with a dead time of ∼0.5 s.

Wolf 359 has a high proper motion due to its proximity, with $\mu_\alpha = -3866.338 \pm 0.081$ mas yr^{-1} and $\mu_\delta = -2699.215 \pm 0.069$ mas yr^{-1} (Gaia Collaboration et al. 2021). Figure 1 displays its position in four epochs, three recorded by the Digital Sky Survey in years 1953, 1988, and 1995, whereas the last one was taken in 2020 reported in this work.

No attempt was made to synchronize the shutter openings of the two telescopes. The different cadences, hence sampling functions, of the two telescopes observing the same flare event in turn provide the possibility to derive the underlined flare profile, which would not have been possible otherwise with a single data set.

Images were processed by the standard procedure of bias, dark, and flat-field corrections. Aperture photometry was then performed using SExtractor (Bertin & Arnouts 1996, 2010) with an adaptive aperture to measure the brightness of Wolf 359 with an aperture size of 4–8 pixels for the NOWT images and of 8–9 pixels for the TAOS images. Figure 2 shows an illustrative image taken by NOWT and by TAOS reported here with the photometric aperture marked.

No standard star was observed and the brightness is referenced to that of the stellar quiescent state. In every case, two reference stars near Wolf 359 in the same image frame were also measured to assess any variations due to the sky. Figure 3 exhibits the NOWT light curves obtained during the campaign with the individual flare events marked. The major event detected on 2020 April 26 by both NOWT and TAOS telescopes is presented separately in Figure 4. While the reference stars remained steady in brightness, Wolf 359 experienced a brightening of ∼0.65 mag detected by NOWT, and ∼0.38 mag detected by TAOS.

Table 1 summaries the photometric measurements used to plot the light curves in Figure 3. Columns 1, 2, and 3 list, respectively, the calendar date, telescope, and the Heliocentric Julian Date (HJD) of the observation (middle of an exposure). The remaining columns are magnitude and associated error of Wolf 359, and of the two reference stars.

In a total of 27 data hours, 13 flare events were identified visually in the light curves, in accord with the (non)variation of the reference stars at the same time. The flare parameters for each event such as the peak amplitude, the rising and decay timescales were derived, from which the integrated total energy was computed.

2.2. Flare Properties

A flare profile is parameterized with (1) the epoch and amplitude of the observed peak in the light curve, and relative to the peak, (2) the rising timescale, and (3) the decline timescale. Usually (2), signifying the energizing process is relatively fast, whereas (3), relevant to the cooling mechanism drops off slower, typified by an exponential or a power-law decay.

First, the observed light curve in unit of flux (count) $f(t)$ is subtracted of then divided by the detrended quiescent stellar count (a linear fit to the flux away from an event) within the spectral filter f_0. To compute the released energy from such a normalized light curve, $\Delta f/f_0 = (f(t) - f_0)/f_0)$, we follow the equivalent duration method described by Gershberg (1972). The flare is approximated by a typical blackbody of effective temperature $T_{\rm flare}$ of 9000 K (Mochnacki & Zirin 1980), thereby having a bolometric luminosity of

$$L_{\rm flare} = \sigma A_{\rm flare} T_{\rm flare}^4,$$

where σ is the Stefan-Boltzmann constant, and $A_{\rm flare}$ is the flare area, related to the observed flare luminosity as

$$L'_{\rm flare} = A_{\rm flare} \int B_\lambda(T_{\rm flare})\, R_\lambda d\lambda.$$

Here $B_\lambda(T)$ is the Planck function and R_λ is the spectral response function for which only the filter response is considered. The observed photospheric luminosity of a star of

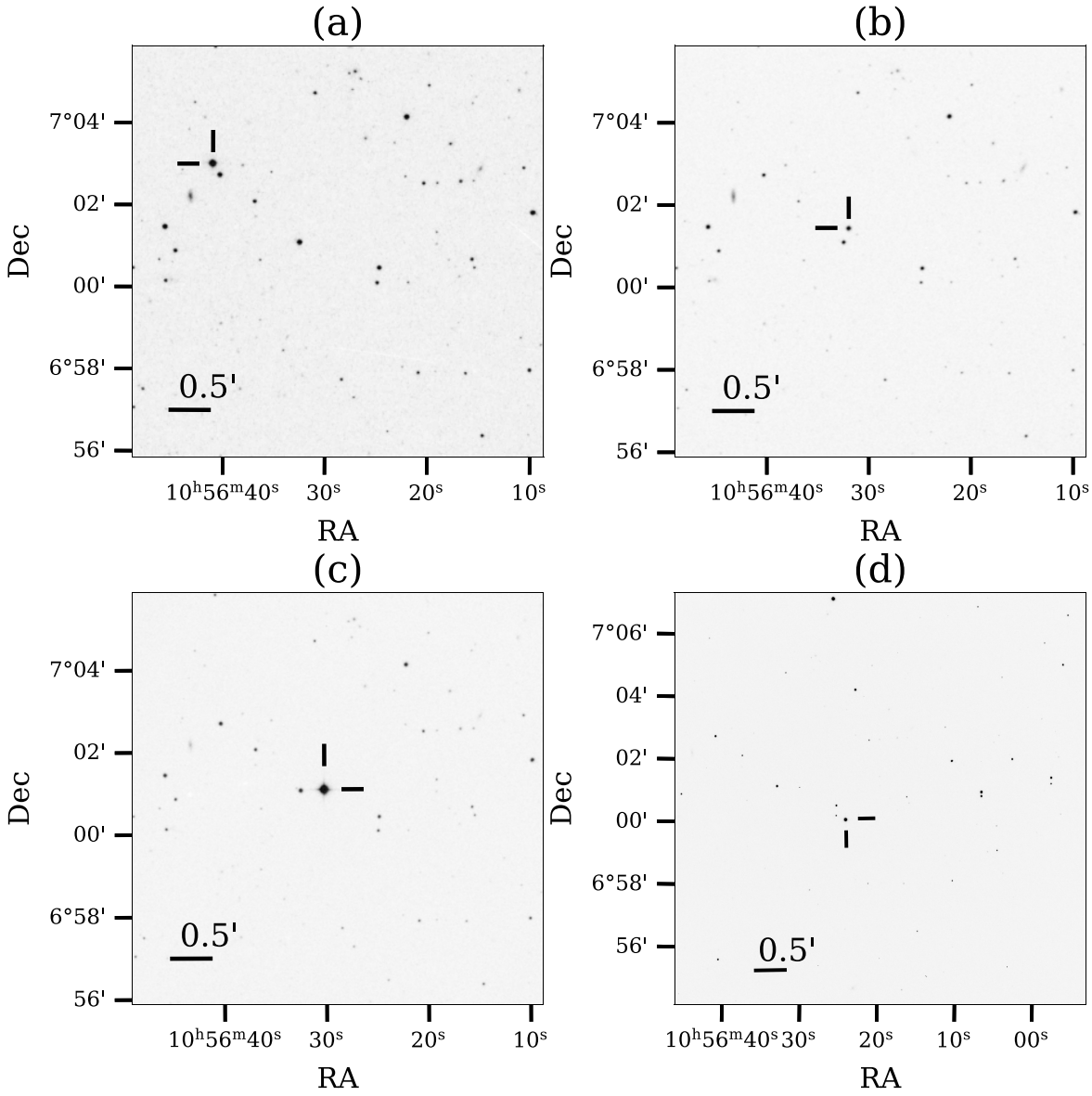

Figure 1. The motion of Wolf 359. The first three images are from Digital Sky Survey taken in (a) 1953, (b) 1988, and (c) 1995, whereas the last image (d) was taken in 2020 as a part of this work, all shown with J2000 coordinates.

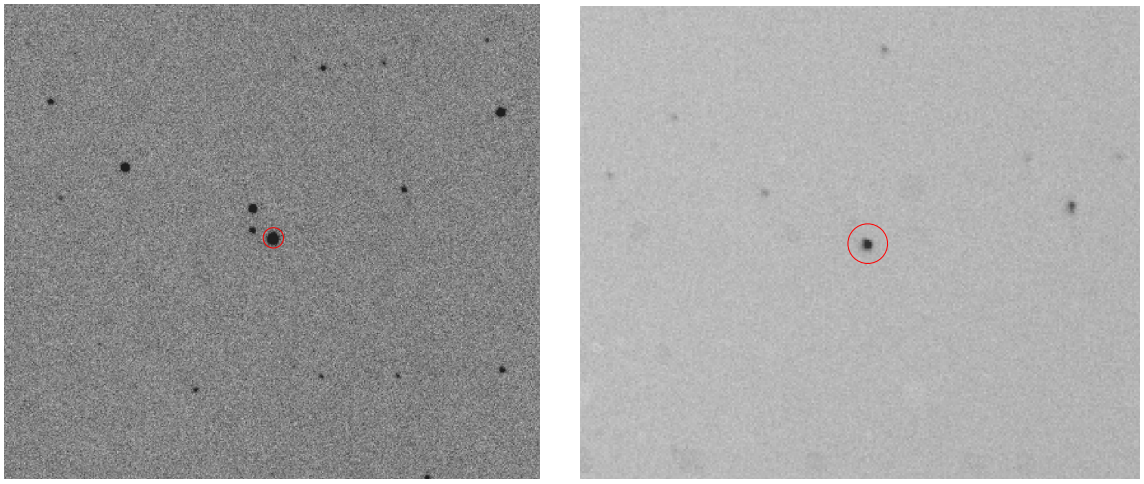

Figure 2. Example images with Wolf 359 each marked with a red circle depicting the maximal photometric aperture size used in light-curve extraction: eight pixels for NOWT (left image), and nine pixels for TAOS (right image).

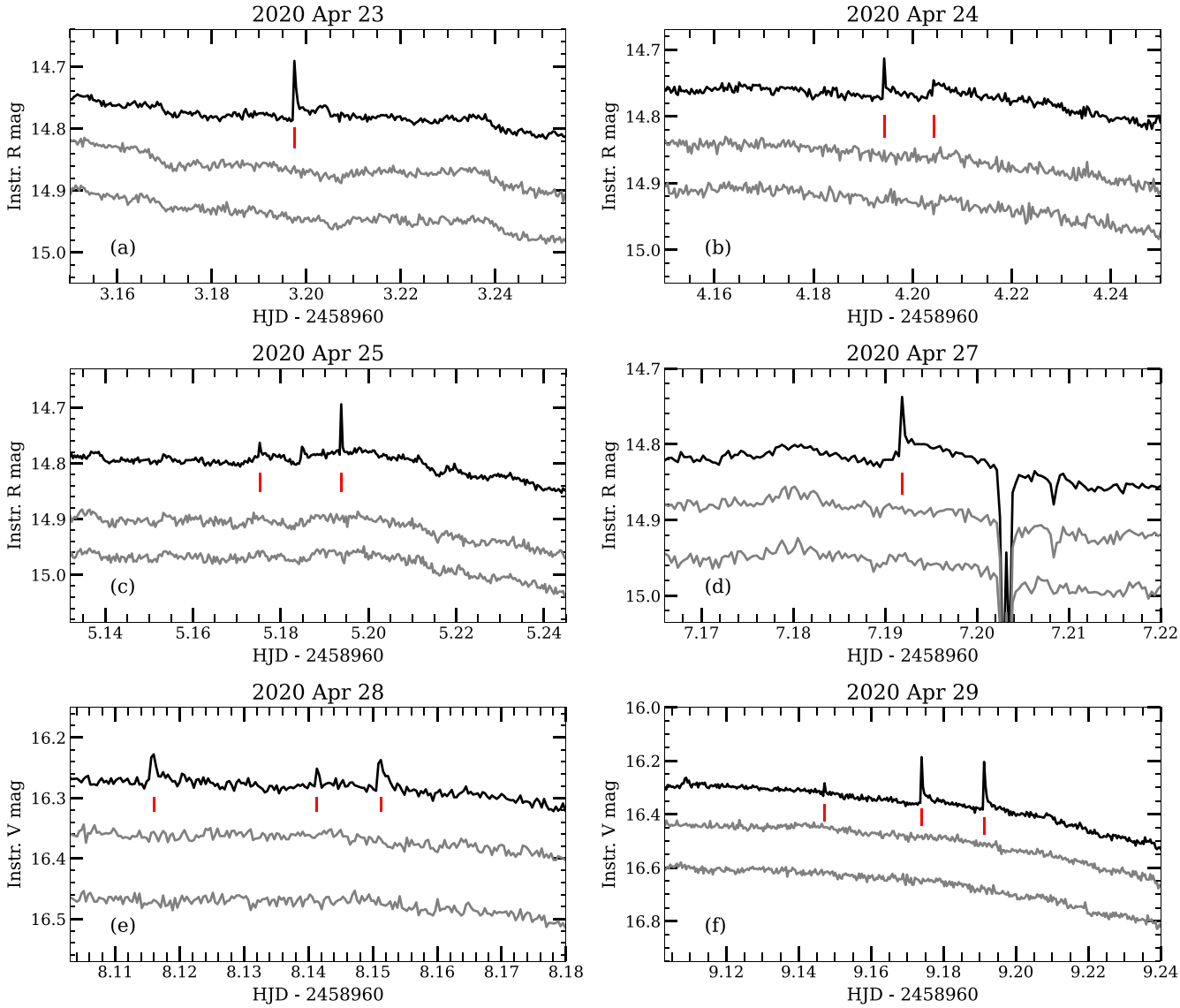

Figure 3. The NOWT light curves of Wolf 359 (in black) and of the two reference stars (in gray). Each flare event detected is marked by a vertical red line. The observations from April 23 to 27 were taken in the *R* band, whereas on April 28 and 29 they were in *V*. The sudden flux drop on April 27 around HJD 2458967.2 was due to weather conditions, manifest also in the reference light curves. The major event on 2020 April 26 detected also with TAOS was analyzed separately and not shown here.

radius R_* is then

$$L_*^{'} = \pi R_*^2 \int B_\lambda(T_*)\, R_\lambda d\lambda.$$

The ratio of $L'_{\rm flare}$ to $L'*$ is the amplitude,

$$C'_{\rm flare} = \frac{\Delta f}{f_0} = \frac{L'_{\rm flare}}{L_*^{'}},$$

and the area of the flare becomes

$$A_{\rm flare} = \pi R_*^2\, C'_{\rm flare} \frac{\int B_\lambda(T_*) R_\lambda d\lambda}{\int B_\lambda(T_{\rm flare}) R_\lambda d\lambda},$$

with the flare luminosity being computed as,

$$L_{\rm flare} = \frac{1}{4} L_* \left(\frac{T_{\rm flare}}{T_*}\right)^4 C_{\rm flare}^{'} \frac{\int B_\lambda(T_*) R_\lambda d\lambda}{\int B_\lambda(T_{\rm flare}) R_\lambda d\lambda}.$$

Finally the total flare energy is estimated from the bolometric luminosity of the star multiplied by the equivalent duration

$$E_{\rm flare} = \alpha L_* \int \frac{\Delta f}{f_0} dt, \quad (1)$$

where α is the constant accounting for the correction for the blackbody assumption and the filter response. Taking the stellar temperature as 2900 K (Fuhrmeister et al. 2005), α of 0.11 for the standard Johnson–Cousins *R* filter, and 0.05 for the *V* filter, Equation (1), adopting $\log L_*/L_\odot = -2.95 \pm 0.05$ (Pavlenko et al. 2006), leads to the derivation of the flare energy, $E_{\rm flare}$ released in an event. Note that this method assumes the flare temperature to be constant throughout the event, and the behavior of the flare is the same in all spectral bands.

Table 2 summarizes the parameters of the 13 events including the superflare detected simultaneously by two telescopes. For all events reported here, the rising time is less than ~30 s, i.e., shorter than the cadence of each of the

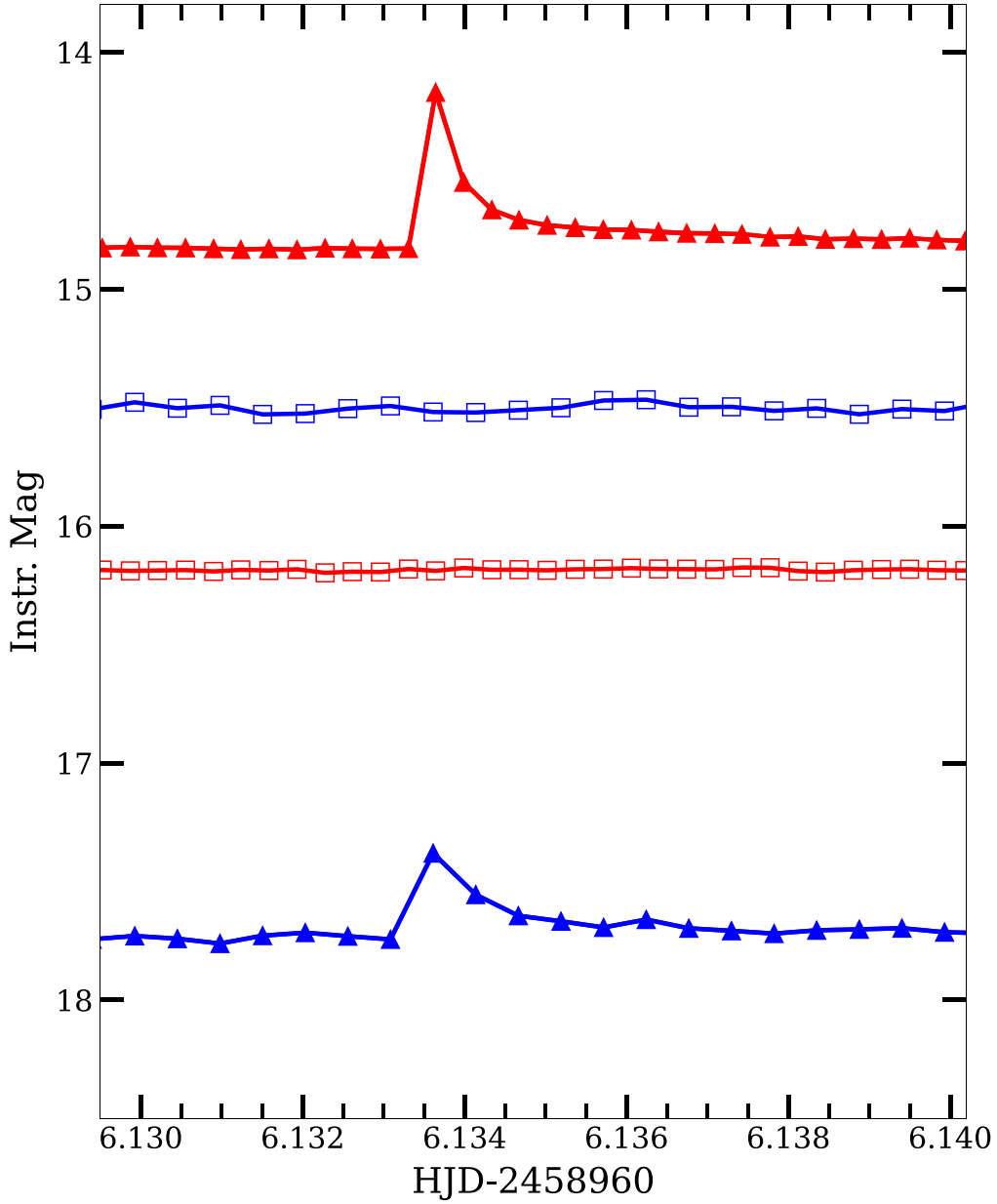

Figure 4. The major event detected on 2020 April 26 by both NOWT (in red) and TAOS (in blue). For each telescope, the measured instrumental magnitudes of Wolf 359 and of a comparison star are displayed to validate the variability. Typical photometric errors are about 0.01 mag so smaller than the sizes of the symbols.

telescopes, so was not derived. This rising/heating timescale is contrasted to those of several minutes among solar-type flares (Yan et al. 2021). In our analysis, the light curve then takes a straight line from the stellar quiescent state, i.e., one data point prior to the peak. The date/time refers to the middle of the exposure within which a flare occurred. The duration of an event is estimated from one data point prior to the peak to where the light curve falls below the uncertainty in $\Delta f/f_0$, typically 0.002 for NOWT and 0.01 for TAOS. The determination of duration time therefore is somewhat subjective, but serves to gauge the relative time length of an event. The events had energies ranging from $\sim 3 \times 10^{29}$ to $\sim 3 \times 10^{31}$ erg, lasting for a couple of minutes to over 20 minutes. Our campaign was not long enough to catch more powerful, presumably rarer events.

We note that the term "superflare" is applicable to solar events, but not well defined for stars, whether it refers to total released energy (in unit of energy) or relative to stellar photospheric luminosity (in unit of power). A superflare of solar-type stars releases 10^{33}–10^{38} erg (Schaefer et al. 2000), which given a typical duration of ~30 minutes (Yan et al. 2021) amounts to a ratio to stellar luminosity $10^{-4}\,L_\odot \lesssim L_{\rm flare} \lesssim 10^{1}\,L_\odot$. An M-dwarf flare, on the other hand, gives out a total energy, 10^{31}–10^{34} erg, with the fast rotators liberating more, up to 10^{35} erg (Lin et al. 2021). For the events reported here, the most energetic one has $E \sim 3 \times 10^{31}$ erg within ~25 minutes, hence with $L_* = 1.1 \times 10^{-3}\,L_\odot$ for the star, leading to $L_{\rm flare}/L_* \approx 0.5\%$. The two-telescope event is powerful, having the rising and exponential decay timescales both less than about 30 s, with a peak amplitude comparable to the stellar flux, we refer this major event as a superflare.

Table 1
Photometric Data for Wolf 359 and Reference Stars

Date	Telescope	Epoch HJD	m_W[a] mag	σ_{m_W}[a] mag	m_1[b] mag	σ_{m_1}[b] mag	m_2[c] mag	σ_{m_2}[c] mag
2020 April 23	NOWT	2458963.1156348	14.7537	0.0016	16.1537	0.0032	16.1891	0.0033
		2458963.1169079	14.7529	0.0019	16.1874	0.0040	16.1823	0.0041
		2458963.1181114	14.7546	0.0019	16.1804	0.0040	16.1860	0.0040
		2458963.1184702	14.7455	0.0019	16.1843	0.0040	16.1740	0.0041
		2458963.1188406	14.7506	0.0019	16.1736	0.0039	16.1807	0.0040
		2458963.1192110	14.7538	0.0019	16.1769	0.0040	16.1817	0.0040
		2458963.1195697	14.7526	0.0019	16.1965	0.0040	16.1828	0.0040
		2458963.1199400	14.7478	0.0019	16.1916	0.0040	16.1856	0.0041
		2458963.1203104	14.7497	0.0019	16.1996	0.0041	16.1905	0.0041

Notes. Table 1 is published in its entirety in the machine-readable format. A portion is shown here for guidance regarding its form and content.
[a] The variable m_W is the magnitude of Wolf 359.
[b] The variable m_1 is the magnitude of reference star 1.
[c] The variable m_2 is the magnitude of reference star 2.

Table 2
Flare Event Parameters

Date/Time HJD−2458960	Amplitude ($\Delta f/f_0$)	Energy (erg)	Time Constant (s)	Duration (s)
3.1974805	0.09	5.68×10^{30}	61	698
4.1942563	0.05	1.48×10^{30}	61	534
4.2042208	0.02	4.46×10^{30}	457	1248
5.1751989	0.03	3.47×10^{30}	15	712
5.1937739	0.09	4.72×10^{30}	12	772
6.1336424	0.82	3.28×10^{31}	23	1515
6.1336110[a]	0.41	3.26×10^{31}	43	1319
7.1918455	0.08	6.64×10^{30}	34	745
8.1159728	0.04	1.08×10^{30}	83	350
8.1413180	0.03	2.87×10^{29}	35	126
8.1512477	0.05	8.30×10^{29}	98	254
9.1471391	0.04	2.79×10^{29}	23	126
9.1739656	0.17	3.18×10^{30}	35	603
9.1912327	0.18	3.38×10^{30}	47	539

Notes.
[a] Measured also by TAOS; all others by NOWT only.

3. The Flare Rate of Wolf 359

The flare rate we detected, 13 flares in 27 hr, equivalent to about 48 events per 100 hr, is consistent with literature results (e.g., Nelson et al. 1979; 47/100 in radio wavelengths). In terms of energetics, Figure 5 presents the cumulative frequency distribution of the flares of Wolf 359 listed in Table 2. Fitted with a power law, $\log \nu \propto \beta \log E$, where ν is the flare frequency distribution with energy greater than E (Hunt-Walker et al. 2012), the index $\beta = -0.87 \pm 0.19$ if the data at the lowest-energy end, incomplete in our experiment, are excluded. Even with our limited number of events, spanning two orders of magnitude in energy, the distribution seems more complex than a single power law, a conclusion that has been drawn for this star and for active M dwarfs in general (Lin et al. 2021). By and large, Wolf 359 produces a flare as powerful as 10^{30} erg approximately once every three hours. While a fast rotating M dwarf like Wolf 359 tends to produce frequent and powerful flares (Lin et al. 2019), it is not known whether the boosted magnetic activity of our target is linked to its own rapid spin alone or to the close-in planet with an enlarged emission volume.

A more energetic flare conceivably would take a longer time to dissipate. Because a flare profile may be complex (e.g., more than a simple exponential or power-law decay, or multiple flares in the light-curve segment), we correlate the duration of a flare with energy, exhibited also in Figure 5. A log–log linear fit gives $t_{\rm flare} \propto E_{\rm flare}^{0.49 \pm 0.08}$. Maehara et al. (2015) related the magnetic reconnection timescale to the Alvén time and derived analytically for solar-type stars, $t_{\rm flare} \propto E_{\rm flare}^{1/3}$, to be comparable to their observed slope of 0.39 ± 0.03. Such a duration-energy relation is also observed in the active dM 4e dwarf GJ 1243 (Hawley et al. 2014; of a slope about 0.4, reading from their Figure 10), and in other M dwarfs (Raetz et al. 2020). Our slope is marginally steeper but, given the incompleteness for weaker events, should be overestimated. If so, this indicates a similar energizing mechanism in M dwarfs as in solar-type stars.

4. Intrinsic Flare Profile Derived from Two-telescope Light Curves

The simultaneous detection of the same event with different sampling functions allows us to break the parameter degeneracy and thereby to infer the underlined flare profile. By varying profile parameters, the light curve that would have resulted for a given sampling function of a telescope is compared with what was actually observed. The profile that yields the least deviation in the chi-squared sense in the two light curves, is considered the "best" solution, closer to the "truth" than any individual observed light curve alone.

The normalized light curves by the two telescopes are displayed in Figure 6. Note that NOWT detects a relative amplitude of ∼0.8, whereas TAOS detects an amplitude of ∼0.4. There is a caveat that, because of the different filters used, f_0 differs for each telescope. Conceivably, the star itself is red in color, but the flare should be relatively blue, but here we assume the same f_0 to normalize each light curve. The peak of the flare was sampled differently: TAOS detected it at HJD of 2458966.133611, whereas NOWT detected it at HJD of 2458966.1336424, with an offset of about 2.7 s.

The sampling effects on an intrinsically continuous function include the integration time (averaging the signal), dead time (no signal), and the lapse, i.e., the offset time between the peak relative to the sampling window. It is this offset and finite sampling time that smear off the peak of the flare and distort the shape of a light curve, accounting for different flare statistics

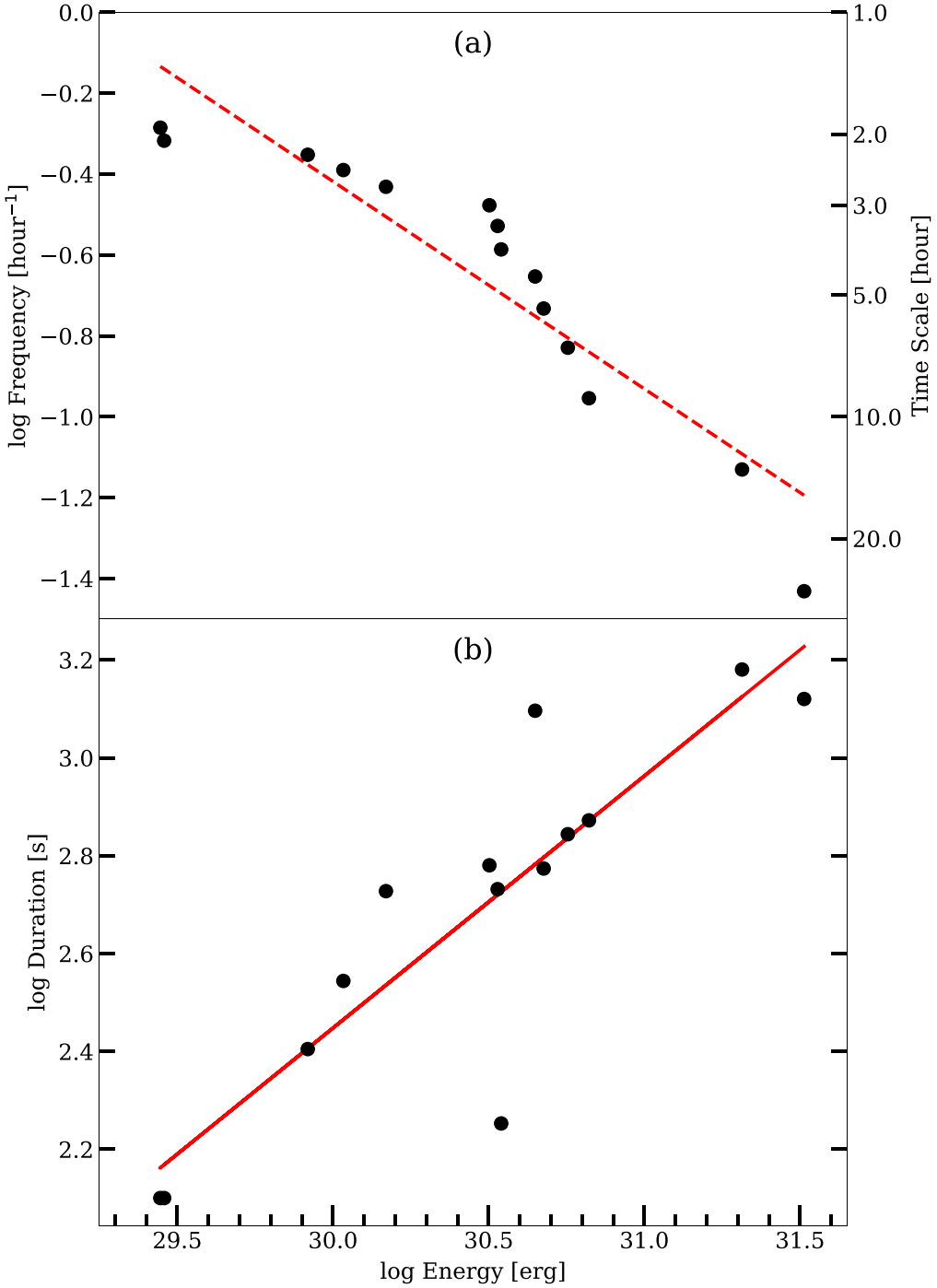

Figure 5. (a) Cumulative frequency (or occurrence timescale) distribution and (b) duration vs. flare energy of the Wolf 359 flares reported in this work. The dashed line in (a) is not meant for a fit but for illustration only because the data seem more complex than a linear fit.

between the long-cadence versus short-cadence K2 light curves (e.g., Raetz et al. 2020; Lin et al. 2021). A grid of event parameters were used to compute the simulated light curves with steps of 0.01 in the peak amplitude and 1 s in decay timescale, chosen as the appropriate step parameters with extensive simulations. For the decay portion, different models were exercised: a single-exponential function ($A\,e^{-t/\tau_1}$), a double-exponential function ($A\,e^{-t/\tau_1} + B\,e^{-t/\tau_2}$), and a power-law falloff ($A\,t^{-\gamma}$), where A and B are amplitudes, t is time, τ_1 and τ_2 are correspondent exponential time constants, and γ is the power-law exponent index. In each case, the computed light curve according to a specific sampling function was compared with the actual observed one ("observed" minus "computed", "$O-C$") to evaluate the chi-squared value (sum of $(O-C)/O$).

Figure 7 presents the best-fit results, whose parameters are summarized in Table 3. The double-exponential model, adding one more degree of freedom in the fitting, gives an over-all better account than the single-exponential function of the fading part of the light curves, judged by the residual χ^2. This is consistent with the time-resolved flares of another eruptive red dwarf, GJ 1243 (Davenport et al. 2014), and supports the

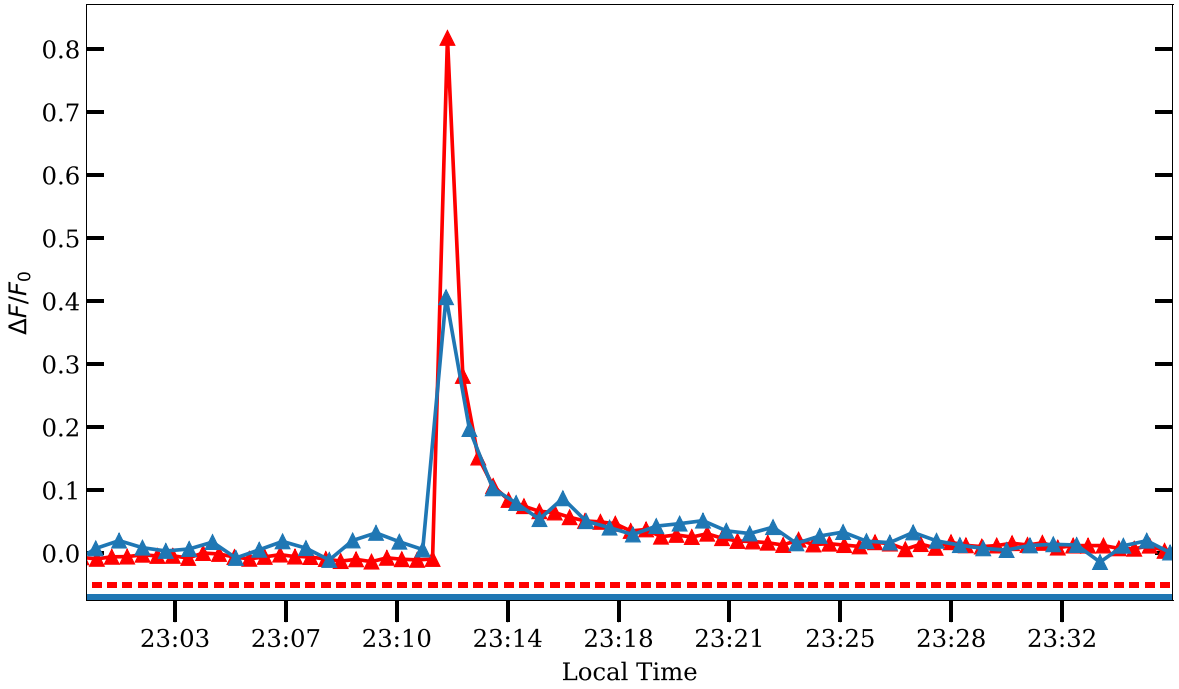

Figure 6. As in Figure 4 for the superflare observed in 2020 April 26, but now each light curve has been detrended and rescaled relative to the quiescent stellar brightness, in flux/count unit instead of magnitude. The horizontal segments mark the sampling function for NOWT (in red) and for TAOS (in blue), with the filled parts for exposure and open (or a dark bar for TAOS) for dead time intervals.

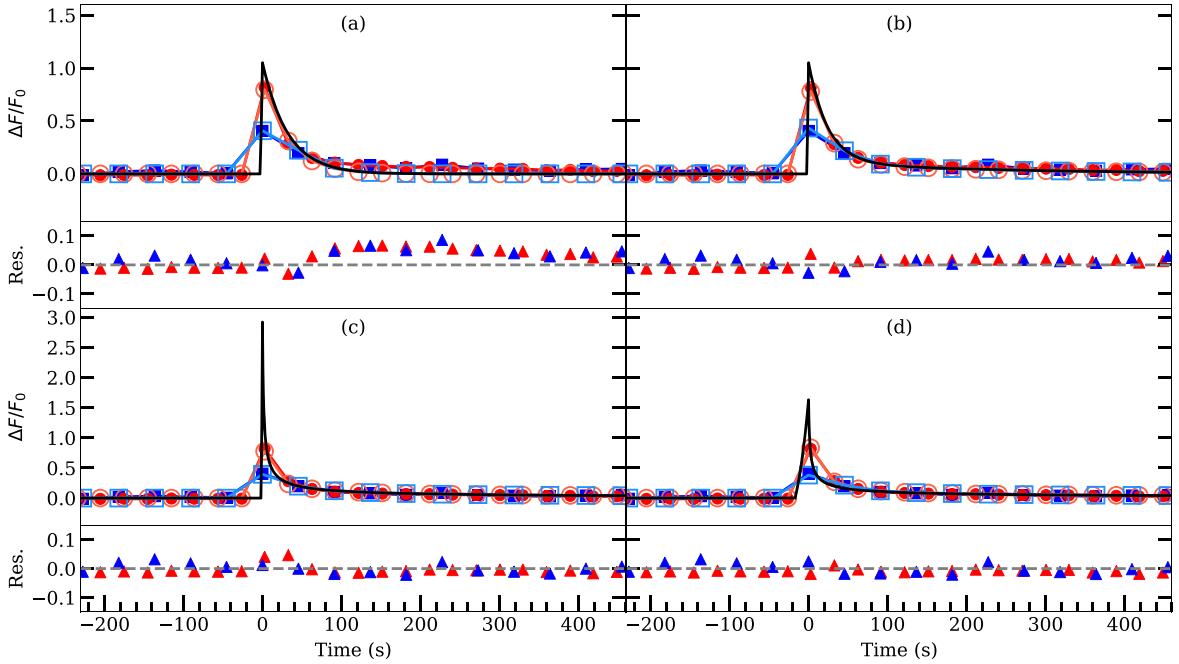

Figure 7. The observed (filled symbols, NOWT in red and TAOS in blue) vs. computed (open symbols) light curves for (a) a single-exponential, (b) a double-exponential, (c) a power-law decay function with an instantaneous impulse rise, and (d) a power-law decay function with a finite-time rise (16 s). For each model, the analytic function is represented as a black curve, and the residuals ($O - C$, the observed minus the computed) are also shown. For (c) the peak amplitude is $\Delta F/F_0 = 2.92$, while in (d) it is $\Delta F/F_0 = 1.63$.

Table 3
Best-fit Model Parameters

Model	A	B	τ_1	τ_2	γ	Energy (erg)	χ^2
One-exponential	1.05		32			5.97×10^{30}	0.014
Two-exponential	0.94	0.11	24	234		8.41×10^{30}	0.007
Power law	2.92				0.7	1.88×10^{31}	0.011
Power law	1.63				0.6	2.06×10^{31}	0.004

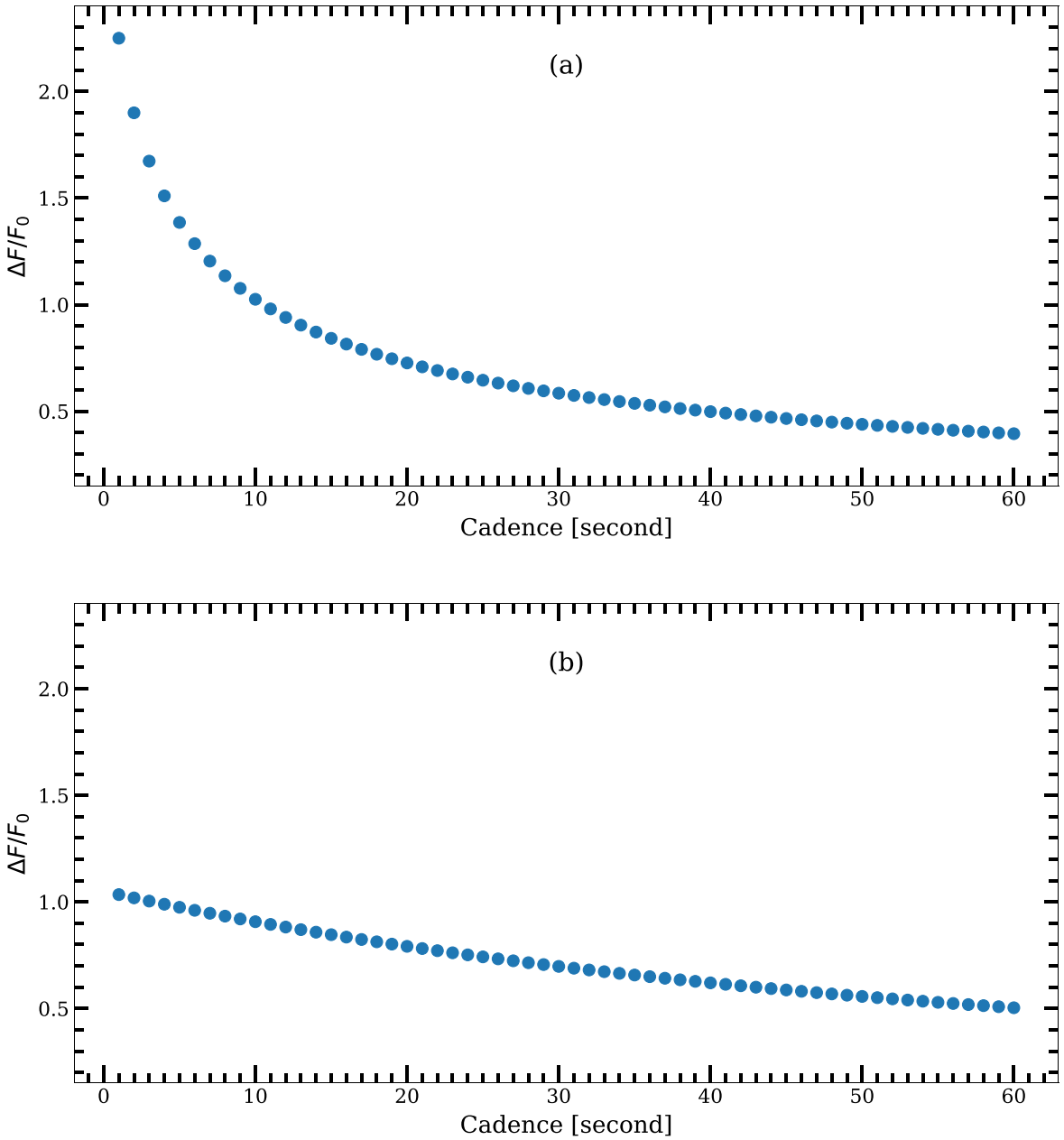

Figure 8. Effect of observing cadence of a continuous (a) power-law, or (b) a double-exponential function.

notion of possibly more than one cooling mechanism (radiative and conductive; Benz & Güdel 2010).

For the power-law model, we present two cases, one with an instantaneous impulse rise, and the other with a finite-time rise. The latter is more realistic, but our data could not constrain the rising timescale. Therefore an exponential rise of 16 s is adopted here as an example, for which a peak of 1.63 times of the stellar brightness is required to fit the data, whereas for an instantaneous rise, the peak would have been 2.92 then falling off faster (with a slightly larger value of γ). In general a power-law decay requires a higher peak than an exponential model, leading to an elevated total flare energy. In our data, the impulse plus the rapid decay portion of the light curve spans no more than a few data points. This means that a higher time resolution is needed than reported here in order to distinguish one cooling function from another.

5. Implication for Flare Observations

A flare event, detected either visually or by an algorithm (e.g., to recognize in a light curve an abrupt rise followed by a few data points above quiescence) is characterized by the amplitude and duration, from which the total energy is derive. The fact that the true superflare event reaches to at least 1.6 times of stellar brightness, while the observed light curves peak, respectively, at 0.8 and 0.4 times, as demonstrated in this work, manifests how the sampling function affects the amplitude of an observed flare. The experimental design to detect sporadic stellar flares hence pertains to an integration time as short as possible so as to resolve the flare profile given the kind of flare events targeted for detection, while commensurate with a sufficient signal-to-noise ratio. Figure 8 plots how cadence affects the detected amplitude of the superflare event reported here, for which the peak of 1.6 times

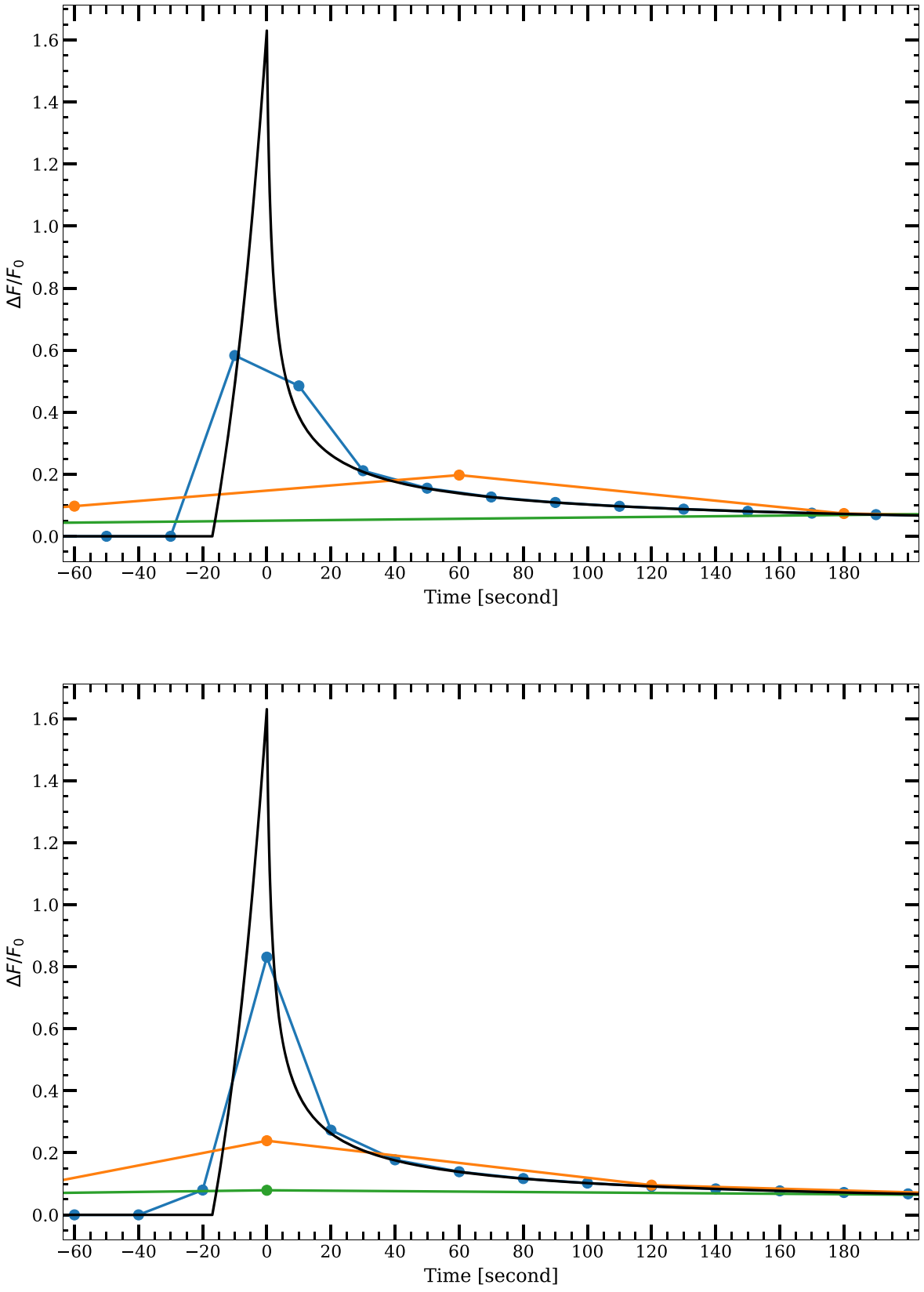

Figure 9. The computed light curves of the intrinsic flare profile with a peak of 1.6 times of the stellar brightness (Figure 7(d)) sampled at a cadence of 20 s (in blue), 2 minutes (in orange), and 20 minutes (in green); (a) with a zero phase lag, or (b) with a 0.5 phase lag.

of stellar brightness would be degraded quickly; e.g., with a 30 s integration the detected peak drops to less than 70%. This applies only to the specific event detected on 2020 April 26 for Wolf 359, but serves to demonstrate vividly the essence of fast sampling. The lesson is while the total energy of a flare can be reasonably estimated with a single data set, different samplings

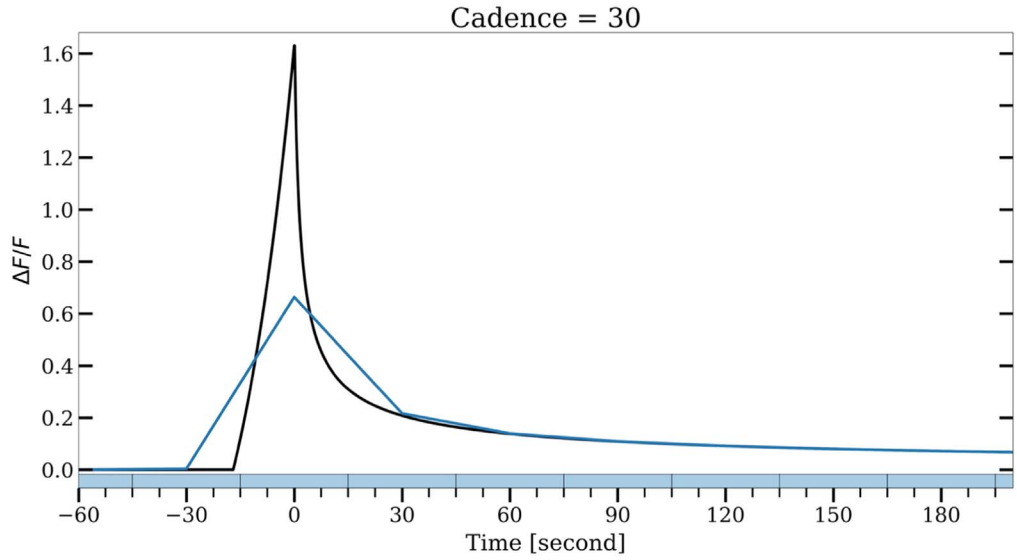

Figure 10. An animation illustrating the effect of discrete sampling of a continuous flare profile. The animation runs from a cadence of 1–30 s to sample the profile in Figure 9, i.e., of a peak of 1.63 with a phase shift of 0.5. The run time duration of the animation is 15 s.

(An animation of this figure is available.)

of a flare is necessary to derive the true profile in order to distinguish the heating and cooling processes. One improvement of our experiment, other than with larger telescopes to afford faster cadences, is to measure the same event at different passbands, or better yet with spectroscopy, thereby diagnosing the temperature variation during the flare.

Stellar flare activity may be elevated if the field lines have an external source to anchor to, be it a circumstellar disk, a companion, or an exoplanet, increasing the magnetic filling factors hence the emitting volume than by surface starspot pairs or coronal loops (Benz & Güdel 2010). In stars like Wolf 359 there may well be a combination of solar-type surface flares plus inflated star-planet events. Long-term high-cadenced monitoring observations are called for to derive any possible rotation or orbital periodicity.

As in the case of Kepler/K2, the Transiting Exoplanet Survey Satellite (TESS; Ricker et al. 2015) provides data as useful for stellar flare research as in the primary science in exoplanets, particularly if complemented with ground-based observations of high sampling rates (e.g., Howard et al. 2020). TESS are monitoring some bright stars of three different cadences: 20 s, 2 minutes, and 10 minutes. Figure 9 illustrates how these three sampling rates would have detected the April 26 event. Here a peak amplitude of 1.6 times of the stellar brightness is adopted (see Figure 7(d)) with a zero phase lag, i.e., with the peak coinciding with the start of the sampling window, versus with a 0.5 phase lag. One sees that for this particular flare only the shortest (20 s) cadence, similar to the data reported here, can resolve the profile, with a phase-dependent amplitude of 0.6 or 0.8, respectively, but neither the 2 minutes (for selected targets) nor the 10 minutes (for the whole frame) cadence can. Figure 10 presents an animation of discrete sampling of a continuous flare profile shown in Figure 9.

In summary, our photometric monitoring of the red dwarf Wolf 359 in 2020 April detected, in 27 data hours, 13 flare events with released energy in the range $\approx 3 \times 10^{29}$–3×10^{31} erg, consistent with the flare occurrence rate for this star reported previously in the literature. For any single-telescope data, the peak and energy are underestimated as the result of sampling by finite integration time with a phase lapse. A major flare was detected simultaneously by two telescopes on 2020 April 26, for which the underlying flare profile is estimated. The profile parameters are model dependent, but the "true" flare amplitude might reach as high as 1.6 times of the quiescent stellar flux, whereas the two telescopes detected a peak level of 0.8 and 0.4, respectively, with the total released energy nearly four times as large.

We thank the referee for constructive comments to improve the quality of the paper. We are grateful to Xinjiang Astronomical Observatory for support in installation and operations of the TAOS telescopes in Qitai. The XAO authors acknowledge the financial aid from National Natural Science Foundation of China under grant U2031204. The relocation of the two TAOS telescopes was funded by the grant MOST 105-2119-M-008-028-MY3. The work at NCU is financially supported in part by the grant MOST 109-2112-M-008-015-MY3.

ORCID iDs

Wen-Ping Chen https://orcid.org/0000-0003-0262-272X
Jinzhong Liu https://orcid.org/0000-0002-7420-6744
Xuan Zhang https://orcid.org/0000-0002-5750-8177
Yu Zhang https://orcid.org/0000-0001-7134-2874
Andrew Wang https://orcid.org/0000-0003-4708-5964
Shiang-Yu Wang https://orcid.org/0000-0001-6491-1901
Matthew J. Lehner https://orcid.org/0000-0003-4077-0985
Anli Tsai https://orcid.org/0000-0002-3211-4219
Chia-Lung Lin https://orcid.org/0000-0001-5989-7594

References

Alcock, C., Dave, R., Giammarco, J., et al. 2003, EM&P, 92, 459
Audard, M., Güdel, M., Drake, J. J., & Kashyap, V. L. 2000, ApJ, 541, 396
Benz, A. O., & Güdel, M. 2010, ARA&A, 48, 241
Bertin, E., & Arnouts, S. 1996, A&AS, 117, 393
Bertin, E., & Arnouts, S. 2010, SExtractor: Source Extractor, Astrophysics Source Code Library, ascl:1010.064

Davenport, J. R. A., Hawley, S. L., Hebb, L., et al. 2014, ApJ, 797, 122
Feigelson, E. D., & Montmerle, T. 1999, ARA&A, 37, 363
Feinstein, A. D., Montet, B. T., Ansdell, M., et al. 2020, AJ, 160, 219
Fuhrmeister, B., Schmitt, J. H. M. M., & Hauschildt, P. H. 2005, A&A, 439, 1137
Gaia Collaboration, Brown, A. G. A., Vallenari, A., et al. 2021, A&A, 649, A1
Gershberg, R. E. 1972, Ap&SS, 19, 75
Guinan, E. F., & Engle, S. G. 2018, RNAAS, 2, 1
Hawley, S. L., Davenport, J. R. A., Kowalski, A. F., et al. 2014, ApJ, 797, 121
Hayashi, M. R., Shibata, K., & Matsumoto, R. 1996, ApJL, 468, L37
Howard, W. S., Corbett, H., Law, N. M., et al. 2020, ApJ, 895, 140
Hunt-Walker, N. M., Hilton, E. J., Kowalski, A. F., Hawley, S. L., & Matthews, J. M. 2012, PASP, 124, 545
Kesseli, A. Y., Kirkpatrick, J. D., Fajardo-Acosta, S. B., et al. 2019, AJ, 157, 63
Klocová, T., Czesla, S., Khalafinejad, S., Wolter, U., & Schmitt, J. H. M. M. 2017, A&A, 607, A66
Liefke, C., Fuhrmeister, B., & Schmitt, J. H. M. M. 2010, A&A, 514, A94
Lin, C. L., Ip, W. H., Hou, W. C., Huang, L. C., & Chang, H. Y. 2019, ApJ, 873, 97
Lin, C.-L., Chen, W.-P., Ip, W.-H., et al. 2021, AJ, 162, 11
MacGregor, A. M., Osten, R. A., & Hughes, A. M. 2020, ApJ, 891, 80
Maehara, H., Shibayama, T., Notsu, Y., et al. 2015, EP&S, 67, 59
Mochnacki, S. W., & Zirin, H. 1980, ApJL, 239, L27
Nelson, G. J., Robinson, R. D., Slee, O. B., et al. 1979, MNRAS, 187, 405
Pavlenko, Y. V., Jones, H. R. A., Lyubchik, Y., Tennyson, J., & Pinfield, D. J. 2006, A&A, 447, 709
Raetz, S., Stelzer, B., Damasso, M., & Scholz, A. 2020, A&A, 637, A22
Ricker, G. R., Winn, J. N., Vanderspek, R., et al. 2015, JATIS, 1, 014003
Rutledge, R. E., Basri, G., Martín, E. L., & Bildsten, L. 2000, ApJL, 538, L141
Schaefer, B. E., King, J. R., & Deliyannis, C. P. 2000, ApJ, 529, 1026
Shibata, K., & Magara, T. 2011, LRSP, 8, 6
Tuomi, M., Jones, H. R. A., Butler, R. P., et al. 2019, arXiv:1906.04644
Yan, Y., He, H., Li, C., et al. 2021, MNRAS, 505, L79
Zhang, Z. W., Lehner, M. J., Wang, J. H., et al. 2013, AJ, 146, 14